Mechanisms for Pole Piece Erosion in a 6-kW Magnetically-Shielded Hall Thruster

Benjamin A. Jorns* Christopher Dodson† John Anderson‡
Dan M. Goebel§ Richard R. Hofer¶ Michael Sekerak‖
Alejandro Lopez Ortega** and Ioannis Mikellides††
Jet Propulsion Laboratory, California Institute of Technology, Pasadena, CA 91109

The mechanisms contributing to the erosion of the inner magnetic pole of a 6-kW magnetically shielded Hall thruster are experimentally and numerically investigated. Sputtering from ion bombardment is believed to be the cause of this wear, but the nature and source of the responsible ions remains unknown. Laser induced fluorescence and translating and surface-mounted probes are employed to characterize the flux and energy distribution of ions incident at the inner pole. It is found that the bulk population is comprised of ions originating from the cathode plume and the near field immediately adjacent to the inner pole. These ions have a low average kinetic energy, < 5 eV kinetic, but a high thermal spread in velocity, $\mathbf{T}_i = 10$ eV. Calculations for the erosion at the pole from experimental measurements indicate that the bulk population only accounts for $10 - 25\%$ of the observed erosion. It is postulated that the remainder of the erosion results from a separate population of ions with sufficiently high energy (> 150 V) to cause high sputtering but too low density to be detected experimentally by the plasma diagnostics in this region. The existence for this high energy population is shown to be a consequence of the high plasma potentials downstream of the thruster exit plane that are characteristic of a magnetically-shielded topography. A simulation validated by experimental measurements of the thruster provides further evidence that a high energy ion populations exists with sufficient density to explain the observed erosion.

Nomenclature

a_L	Lindhard screening coefficient
A_p	Probe surface area, m^2
β	Fit parameter
B	Magnetic field magnitude, Gauss
c	Speed of light
c_s	Ion sound speed, m/s
E	Ion kinetic energy, eV
ϵ	Reduced energy
ε	Erosion rate, μm h^{-1}
f_i	Ion velocity distribution function
T_s	Temperature of particle x, eV
η	Fit parameter
Φ_i	Ion flux, ion m^{-2} s^{-1}

*Engineer, Electric Propulsion Group, AIAA Senior Member, benjamin.a.jorns@jpl.nasa.gov
†JPL Affiliate, Electric Propulsion Group, Doctoral Candidate, UCLA, AIAA Student Member
‡Senior Engineer, Electric Propulsion Group, AIAA Senior Member
§Senior Research Scientist, Thermal and Propulsion Engineering Section, AIAA Fellow
¶Technical Group Lead, Electric Propulsion Group, AIAA Associate Fellow
‖Engineer, Electric Propulsion Group, AIAA Senior Member
**Engineer, Electric Propulsion Group, AIAA Member
††Principal Engineer, Electric Propulsion Group, AIAA Associate Fellow

ρ	Density kg m^{-3}
γ_θ	Angular dependence of sputter yield (Yamamaru), atoms ion^{-1}
q	Fundamental charge
I_{sat}	Ion saturation current
$I(\nu)$	Laser intensity
$i(\nu)$	Atomic transition lineshape
λ	Laser wavelength
M_x	Mass of particle x, amu
m_x	Mass of particle x, amu
n_s	Plasma density of s species, m^{-3}
ν	Laser frequency
ϕ	Plasma potential, V
P	Signal intensity from laser induced fluorescence
r_c	Mean discharge channel radius
s^{KrC}	Kr-C potential nuclear stopping cross-section
θ	Angle with respect to normal of ions incident at pole
$v_{x,y}$	Ion velocity component in the axial (x) and radial (y) directions
Z	Charge state

I. Introduction

The erosion of the magnetic pole pieces by ion sputtering represents one of the major life limiting process for magnetically-shielded Hall thrusters. This is because magnetic shielding eliminates the traditionally dominant form of erosion—the wear of the discharge chamber rings[1–4]—leaving secondary, slower mechanisms such as pole erosion to emerge as the principal concern. Despite a concerted effort to investigate pole erosion in shielded thrusters,[5–8] the nature of this process still remains unclear. This uncertainty poses a risk for deep space applications such as the proposed Asteroid Robotic Redirect Mission (ARRM) that calls for 12.5 kW Hall thrusters with lifetimes extending to 25,000 hours.[9,10] On this timescale, even the slow erosion of the poles represents a potential failure mechanism.[6]

The problem of pole erosion first came to light during a wear test on the magnetically-shielded H6MS Hall thruster at the Jet Propulsion Laboratory (JPL).[11] While this study demonstrated that shielding eliminated the erosion of the thruster's discharge chamber, it also revealed an unexpected sputtering of the iron magnetic poles. A second 150 h campaign on the H6MS to quantify systematically this erosion showed that if the sputtering was caused by normally-incident, singly charged ions, the erosion only could be explained if these ions impacted the poles with an average energy of 156 eV. Significantly, this test also demonstrated that the erosion process was a gradual one where only a 3.5 mm thick pole cover of graphite would provide sufficient life to the H6MS for 50 kh at 6 kW (300 V and 20 A). This result has led to the incorporation of pole covers into the design of the proposed electric propulsion system for ARRM.[10]

The work from Sekerak et al ultimately demonstrated that a non-negligible flux of energetic ions at the pole is necessary to explain measured erosion rates. Understanding pole erosion thus is a question of uncovering the mechanism generating these high energy ions. Numerical studies with Hall thruster models performed to date have provided some insight about the source of energetic ions[7,8] but have not been able to capture the correct erosion rates. There as yet has not been an attempt to elucidate the mechanism through experimental studies. With this in mind, the purpose of this investigation is to examine empirically the role of singly-charged ions in the erosion of the poles. We use a combination of laser induced fluorescence (LIF) and probe diagnostics to measure the ion velocities and flux entering the sheath at the inner pole of the H6MS and apply known sputtering models to estimate the erosion. We ultimately find that the bulk population of ions impacting the pole originates from the near field region and cathode and does not have sufficient energy to explain the observed erosion. We therefore explore an alternative theory—first proposed by Mikellides et al[7]—for erosion in shielded thrusters based on a small population of ions born near the edge of the ion beam fluxing back to the pole. We show from our experimental measurements that there is a path for ions born in this region to return to the pole, and we use a model validated by our experimental measurements to demonstrate that this energetic population has a sufficiently high density to explain the erosion at the pole. Moreover, we find that the density of this beam ion is too low compared to the bulk

population of ions to be resolved by the LIF diagnostic we employed in this experiment. This explains why we did not detect the population with our measurement in the near field.

II. Experimental Setup

A. Thruster and facility

We examined the H6MS,[3,4] 6-kW magnetically shielded Hall thruster for this campaign (Fig. 1). This thruster was adapted from the baselined H6US, a 6-kW thruster jointly developed by the University of Michigan, the Air Force Research Laboratory, and JPL.[12–17] Like the H6US, the magnetically-shielded configuration has a center-mounted LaB6 hollow cathode[18] with iron magnetic pole pieces and a boron nitride discharge chamber. In the H6MS, however, the magnetic field topography is shaped in such a way that a high plasma potential—on the order of the discharge chamber value—is maintained near the discharge chamber walls. This minimizes energetic ion flux to the walls and therefore extends the life of the device.

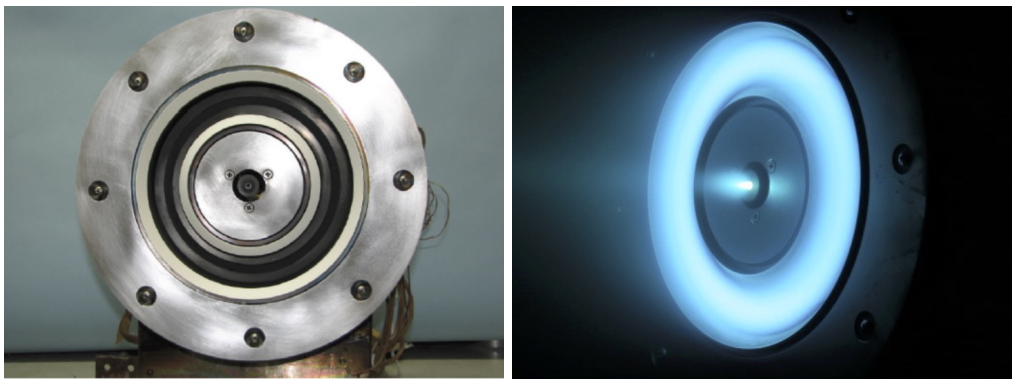

(a) (b)

Figure 1: a) H6MS thruster. b) H6MS operating in the JPL Owens chamber at 300 V and 20 A.

The magnetic shielding of the H6MS discharge chamber was successfully demonstrated in an experimental campaign described in Refs. 4, 11, and the performance and stability of the shielded thruster similarly have been shown to not deviate signficantly from the well-characterized baseline configuration. We operated the thruster at 6 kW with 300 V and 20 A, the same operating point where the pole erosion previously was quantified in a wear test by Sekerek et al.[6] We similarly used the same 7% cathode flow split during testing and connected the thruster chassis to facility ground. At this 6 kW condition, the thrust is 384 mN with a total efficiency of 62.4%.

The H6MS was fired in the Owens vacuum chambered located at JPL. This is a 3 m diameter $\times$ 10 m cryogenically-pumped vacuum chamber lined with graphite paneling. Background chamber pressure was monitored with an ionization gauge located in the chamber wall downstream of the thruster exit plane and two gauges in the plane parallel to the thruster face calibrated for xenon. At the steady-state flow rate of xenon of 19.63 mg/s employed in this experiment, the background pressure of the facility was maintained at 1.3 $\times 10^{-5}$ Torr.

B. Translating probes

We measured the plasma parameters in the near field downstream of the inner pole with a high-speed translating probe system. The system, described in more detail in Ref. 19, consists of a probe arm mounted on a two-axis belt driven stage. Depending on the measured plasma parameter, either a cylindrical Langmuir probe or emissive probe is attached to the probe arm. This element is inserted into the inner pole region from a starting position 5 channel lengths downstream of the pole, and the voltage and current to the tip are recorded as a function of position when the probe passes a location 1.5 channel lengths downstream of the pole. During insertion, the probe reaches a maximum speed of 90 cm/s and stops 3 mm away downstream from the pole. We canvassed the entire region immediately downstream of the inner pole (shown qualitatively in Fig. 2) by inserting it along six longitudinal trajectories parallel to the thruster's central axis. This yielded

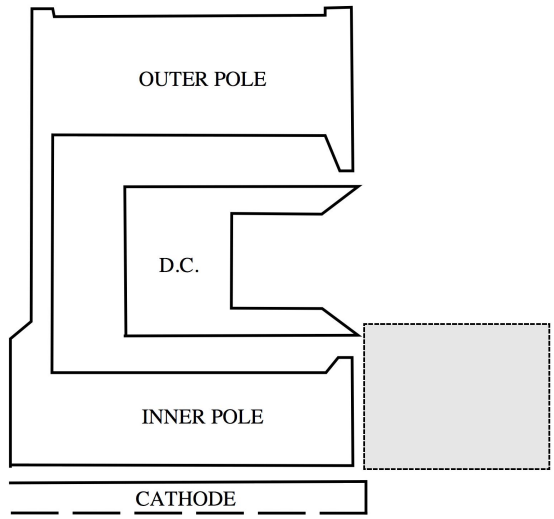

Figure 2: Qualitative schematic of H6MS region showing in highlighted region the probed area adjacent to the inner pole. D.C. denotes discharge chamber.

an axial spatial resolution of approximately 8 mm.

Previous experimental campaigns on the H6US have shown that probe insertion into the discharge chamber of the thruster can result in significant perturbations to the background plasma parameters.[19] These changes are often, though not always, reflected by perturbations to the global operating parameters such as discharge current cathode to ground potential. We monitored both of these global parameters for this campaign and found that they were unperturbed as the probe entered the plasma adjacent to the inner pole. This is not unexpected given the low plasma density in this region and its distance from the the thruster acceleration and ionization zones. We used this result to assert that these near field measurements were relatively unperturbed and that the indicated parameter plasma parameters were accurate.

1. Langmuir probe

We employed a swept cylindrical Langmuir probe for electron temperature measurements during this campaign. This probe was mounted on the end of the translating system's arm and consisted of a 0.25 mm diameter tungsten wire with 2 mm protruding beyond the surrounding alumina insulator. During insertion, we swept the probe from -150 V to 150 V at a rate of 300 Hz. The probe voltage and current were simultaneously recorded at a rate of 150 kHz to generate IV traces as a function of probe position. We injected the probe three times at each radial location and used the same spatially-triggered data acquisition system as described in Ref. 20 to average the data over these shots. We then extracted the the electron temperature by applying the standard exponential fit with an offset.[21] Since the probe was moving during data acquisition, there was a discrete distance between each data point and an inherent spatial uncertainty associated with each measurement. The uncertainty was dictated by how far the probe moved while the data that we used to extract the electron temperature was collected. We found for a given sweep rate an average longitudinal distance between points of 2.5 mm and a spatial uncertainty of ~ 1 mm.

2. Emissive probe

We implemented an emissive probe to measure the plasma potential in the region downstream of the thruster. This probe tip consisted of a 0.127 mm diameter filament bent between two alumina ceramic tubes. Inside the tubes, the filament was spot welded to two tantalum wires. The alumina tubes in turn were secured in a double-barreled boron nitride sheath. The separation between the alumina tubes was 3 mm, and the length of the exposed filament was 2 mm. During testing, we heated the probe tip with a floating supply and recorded the voltage at tip with respect to ground as we inserted in into the plasma downstream of the pole cover. We injected the probe multiple times, incrementing the applied heating current until the measured

spatial dependence of the probe potential did not change with heater power. We then adopted this profile as the space-charge limit for probe emission. In order to correct for the offset incurred by the space-charge limited sheath, we applied a 0.5 T_e correction to the data per $\phi = \phi_{EM} + 0.5\mathrm{T}_e$ where Φ_{EM} is the emissive probe potential. This correction is appropriate in the limit we estimated for the the near field plume plasma where $\mathcal{O}\left(\lambda_{de}/r_p\right) \sim 1$, r_p is the probe radius and λ_{de} is the Debye length.[22] As this correction required our electron temperature measurements, the inherent spatial resolution and uncertainty for the potential measurements were the same as those for the Langmuir probe electron temperature measurements.

C. Surface mounted Faraday probes

Six Faraday probes were mounted on the poles of the H6MS thruster (Fig. 3), three on the inner and three on the outer. For this study, we only report the data for the probes on the inner pole which were located at radial positions $r = 0.375\mathrm{r}_c, 0.49\mathrm{r}_c$, and $0.63\mathrm{r}_c$, where r_c denotes the radial distance from the thruster centerline to the channel centerline. The Faraday probes had planar 3.2 mm ID and 6.4 mm OD guard rings surrounding flat 2.4 mm inner collectors. The probes were positioned facing downstream with their active areas $\sim$ 3 mm from the pole's surface and with their backs insulated so that only current from the downstream direction would be collected. Both the inner collector and guard ring voltages were swept from voltages sufficiently negative for the probes to be in the ion collection regime (on the order of -100 V relative to ground) into the electron collection region (as high as 100 V relative to ground). During data collection, the voltage was swept over the full range in 100 ms and data was obtained at 100 kHz. We extracted the electron temperature from the sweeps by applying the standard exponential fit with an offset,[21] and we determined the ion current density by fitting a line to the IV trace for the values below the floating potential and taking the fit value at 3 T_e below the floating potential. We estimated the error in the current density as the difference between the ion current fit values at 3 T_e and T_e below the floating potential.

D. Laser Induced Fluorescence

1. *Overview and Analysis*

We employed a Laser Induced Fluorescence (LIF) system to measure the ion velocity distribution function of the singly charged xenon ions. This system targets the same strong, non-resonant transition scheme that has been adopted for a number of other Hall thruster studies (c.f. Refs. 23–33). In the ion frame frame of reference, the absorption of light at the near-infrared wavelength 834.953 nm (vacuum) excites the metastable state of Xe II at $5p^2(^3P_2)5d2\,[4]_{7/2}$ to a short-lived intermediate level at $5p^4(^3P_2)6d^2[3]^{\circ}_{5/2}$. This excited state then quickly decays to the configuration $5p^4(^3P_2)6s^2[2]_{3/2}$ fluorescing at 542.066 nm (vacuum) in the green spectrum. In the standard LIF setup, a focused laser beam of intensity $I\left(\nu\right)$ with frequency $\nu = c/\lambda$ intersects a fixed volume V_{int} of plasma, and the intensity of fluoresced light $P\left(\nu\right)$ is recorded. For

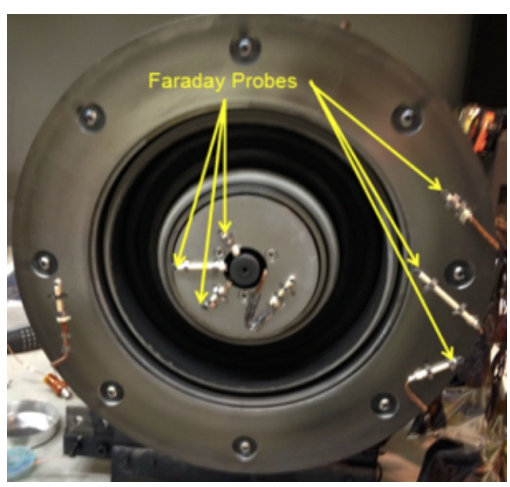

Figure 3: Faraday probe locations on inner and outer H6MS poles.

beam intensities below the saturation limit, the magnitude of the induced fluoresced light is given by

$$P(\nu) \sim V_{int} I(\nu)\, i(\nu) \qquad\qquad i(\nu) = h(\nu) * f_i\left(c\left[\frac{\nu_0}{\nu} - 1\right]\right), \tag{1}$$

where $i(\nu)$ denotes the lineshape of the transition; $h(\nu)$ is the homogenous broadening of the transition lineshape due to effects such as natural line broadening, hyperfine splitting, and the Zeeman effect; ν_0 is the absorption frequency in the rest frame; $f_i(v)$ is the ion velocity distribution function (IVDF) along the direction of the beam; and $*$ denotes the convolution function. By varying the laser frequency while maintaining constant beam intensity and monitoring the fluoresced signal intensity, we find $P(\nu)$ as a function of frequency. Provided the homogenous broadening is small, we then can make the Doppler substitution $v = c(\nu - \nu_0)\nu$ into the raw LIF signal, Eq. 1, to approximate the ion velocity distribution function. We show in this study raw profiles of $P(\nu)$ as a function of velocity in order to illustrative qualitative trends in the IVDFs.

For our quantitative analysis, we examine two macroscopic parameters for the ion velocity inferred from $P(\nu)$, the average ion velocity and the variance. For the average velocity, we take the first moment with respect to velocity to estimate the bulk velocity $\langle v \rangle$ in the beam direction. This method introduces minimal error as the major contributions to $h(\nu)$ are symmetric with respect to ν_0.[34,35] As for the variance, $\sigma^2 = \langle (\langle v \rangle - v)^2 \rangle$, the effect of homogenous broadening can lead to overestimates if the raw LIF profile from Eq. 1 is directly equated to the IVDF. We bound this effect by noting that the strong magnetic field near the pole, $300 - 900$ G, makes the Zeeman effect the dominant contributor to homogenous broadening. The semi-empirical form for this broadening found by Huang[16] is $h(\nu) = \delta(\nu_0 - \alpha B/2) + \delta(\nu_0 + \alpha B/2)$, where δ is the Dirac delta function, B is the magnetic field magnitude, and $\alpha = 2.7273$ MHz/G. In the non-relativistic limit and subject to the assumption of approximately a Maxwellian distribution of ions then, we find that the variance in the ion velocity we estimate from Eq. 1 is related to the actual variance through

$$\langle \sigma \rangle^2 = T_i + m_i \left(\frac{c}{\nu_0}\alpha B\right)^2, \tag{2}$$

where T_i is the effective ion temperature in energy. For the ion temperatures we measured in Sec. III and the corresponding magnetic field magnitude at the pole, we found that with one exception, the Zeeman splitting only introduced a maximum error of 15% if we equated the ion temperature to the variance in the raw LIF signal. We therefore make the assumption $T_i \approx \langle \sigma \rangle^2$ for this study with the caveat in mind that this can lead to an overestimate for predicted erosion (Sec. III). We also note briefly that we examined the response of the measured lineshape as a function of laser intensity and found that at maximum laser power, the transition remained unsaturated.

2. Setup

The airside configuration for the LIF system is shown in Fig. 4. The laser source is a New Focus Velocity TLB-6716 diode laser with a coarse tuning range of 825-855 nm, a fine mode-hop range of $\sim$ 80 GHz, a continuous output power of 15 mW, and a linewidth of 200 kHz. This laser is fiber coupled to a New Focus TA-7616 tapered amplifier capable of amplifying the beam power to a continuous 500 mW into free-space. The output from the tapered amplifier is split into two beams that are passed through two mechanical choppers and then coupled into two 50 um, 0.22 NA multimode fibers. Ten percent of the beam from the amplifier is sampled for diagnostic purposes, passing into a Toptica WS/7 wavemeter (60 MHz accuracy) and a Fabry-Perot scanning etalon.

The vacuum side of the LIF system is shown in Fig 5. The fiber-coupled laser light from both sides of the beam splitter is passed into the Owens chamber through feed throughs and connected to injection optic assemblies (labeled West and East in Fig. 5) that focus the fiber outputs to beam waists in the region of interest near the thruster. Each injection optic consists of a 2.54 cm diameter plano-convex lens positioned with respect to the fiber to yield a beam waist of 2 mm diameter at a distance of 1 m. The two injection optics are located at 45° angles with respect to thruster centerline and aligned so that the beams cross at their waists. This spatial arrangement removes the optics from the thruster beam while still interrogating orthogonal components of the ion velocity distribution function. After alignment and optimization through the vacuum feed through, we measured a maximum power of 120 mW delivered to the 2 mm diameter spot size for the West side optics and a maximum coupled power of 60-80 mW to the East side. This discrepancy in power resulted from variability in the quality of the fiber feedthroughs.

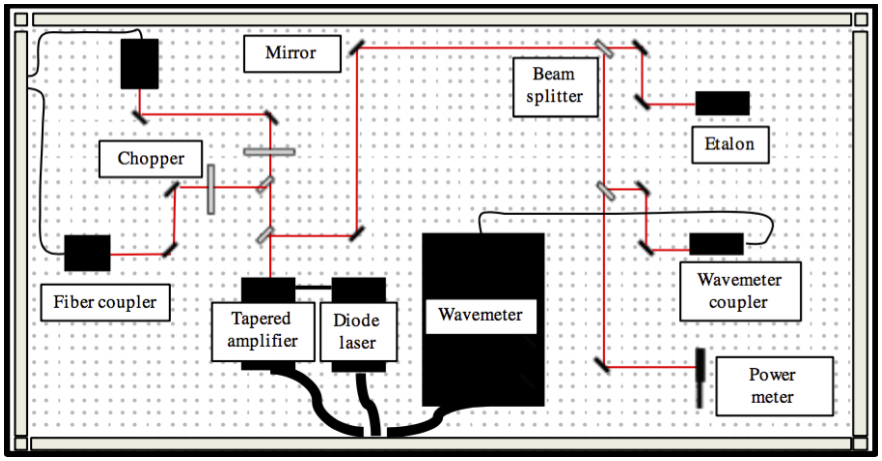

Figure 4: Airside optical table layout for LIF system.

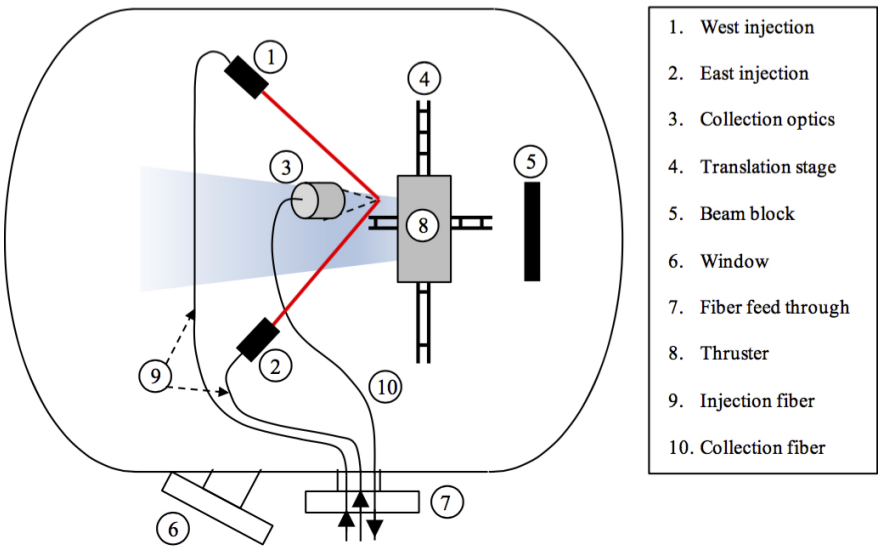

Figure 5: Layout for LIF system in the vacuum chamber. The arrows on the vacuum feedthrough show the flow direction of light: into the chamber for the injection optics and out of the chamber for the collection optic. The collection optic is tilted out of the plane by $\sim 70°$.

We placed the collection optics assembly above the plane of the thruster with its focal length coincident with the beam waist of the injection optics. This assembly is oriented out of the horizontal plane by 70° in order to prevent overlap of the collection volume with reflections of the injected beams from the surface of the iron pole pieces. The collection optic assembly consists of a lens tube with a 600 um NA = 0.22 fiber placed at the focal length of a 76.2 mm diameter plano-convex lens with a 200 mm focal length. A second 76.2 mm diameter lens facing the plasma and collinear with the first lens is positioned with its 200 mm focal length aligned with the intersection of the injection beams. In principle this 1:1 system should yield a collection area at the focal length of 600 um; however, we found that aberrations and imperfect alignment yielded a larger effective collection area of 1.5 mm. Taking into account the oblique angle the collections optic made with the vertical plane and the effective spot size, we estimated the resolution of the optics to be approximately 1.5 mm in the radial direction and 2 mm in the axial direction. The light collected from the fluoresced interrogation volume passes through a chamber feedthrough and then is coupled through a 543 ± 11 nm bandpass optical filter into a Hamamatsu H10721-01 photomultiplier tube. This module converts the absorbed light from the fluoresced signal to a current which is then amplified and passed into

two Stanford Research System 830 lock-in amplifiers. These employ the mechanical chopper frequencies as their references and output the magnitude of the bandpass filtered, amplified signal.

The thruster was mounted on a two-axis translation stage for this campaign. The overlap of the injection beams and collection optics therefore remained fixed in space during testing while we translated the thruster in the axial and radial directions.

3. Operation

For this study, we performed LIF measurements along the channel centerline and near the inner pole. The fluoresced signal from the plasma along the channel centerline was sufficiently high that we could take LIF data from both beams concurrently. The spatial separation data points of these measurements was 4 mm axially. At the pole where the plasma density and temperature were an order of magnitude lower than in the channel, we removed the beam splitter in Fig. 5 and collimated all of the light into one injection axis at a time. This allowed us to generate a higher signal to noise ratio, though it slowed the data collection process. We generated a two-dimensional spatial map of IVDFs for the inner pole campaign in the same region as indicated in Fig. 2. For both configurations, we performed scans by operating the laser in constant power mode and applying a linear ramp in wavelength in the vicinity of the transition line. We recorded the outputs of the SRS lock-in amplifiers as a function of the vacuum wavelength as indicated by the wavemeter. Each scan consisted of 250 data points over an 60 GHz tuning range. The integration time on the lock-in amplifier was 300 ms which translated to 4-5 minutes per scan. The measured LIF signal as a function frequency (Eq. 1) was converted to velocity with the Doppler relation, $v = c\,[\lambda/\lambda_0 - 1]$.

4. Signal to Noise

We employed the LIF diagnostic to generate IVDFs along each injection beam at a number of locations in the near-field region adjacent to the pole. Fig. 6 shows two normalized examples from this campaign that were taken at a position 5 mm downstream of the inner radial edge of the inner pole. The signal to noise for these sample plots is 18 for the West side and 8 for the East side where we have adopted the convention of Huang et al[31] in defining this parameter as the peak value in the IVDF trace to the root mean square of the IVDF at the wings. The reason for the disparity between the signal to noise between the two injection directions was the result of disparate power coupling efficiency we achieved through the fibers. The sparseness of the plasma in the near-pole region yielded low signal to noise ratios raging from 1- 20. For the purposes of this investigation, we only report data where the signal to noise exceeded 5.

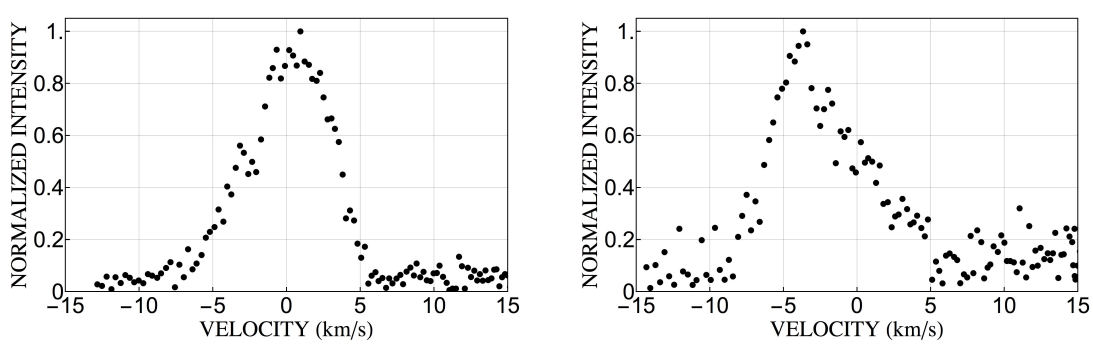

(a) (b)

Figure 6: Raw LIF traces for West (a) and East (b) beam directions at a location 5 mm downstream of the inner radial edge of the inner pole. Each plot is normalized by the maximum intensity.

III. Results

A. Ion trajectories in the near-field

We show in Fig. 7(a) vector maps of the average ion velocities in the near field region. The lengths of the vectors are proportional to speed where the scaling factor depends on the color of the arrow. We generated Fig. 7(a) by calculating the average speed along each beam direction from the corresponding IVDF trace, $\langle v \rangle$. We then rotated the vector formed by these components by 45° to place it in the radial-axial thruster frame of reference. In most cases, there was only one discernible peak in the distribution functions; however, in the region near the thruster channel, there were traces with two distinct peaks with different amplitudes. We assigned two vectors to these locations. Based on the magnitudes of the velocities shown in Fig. 7(a), we have grouped the vectors into two sets. The ions in the first population (blue) are located downstream of the channel and have high velocities, ~ 20 km/s, directed away from the thruster. The second population (black) consists of ions in the near field of the inner pole between the channel and the cathode. These ions have velocities directed back at the pole with slow speed, ~ 2 km/s.

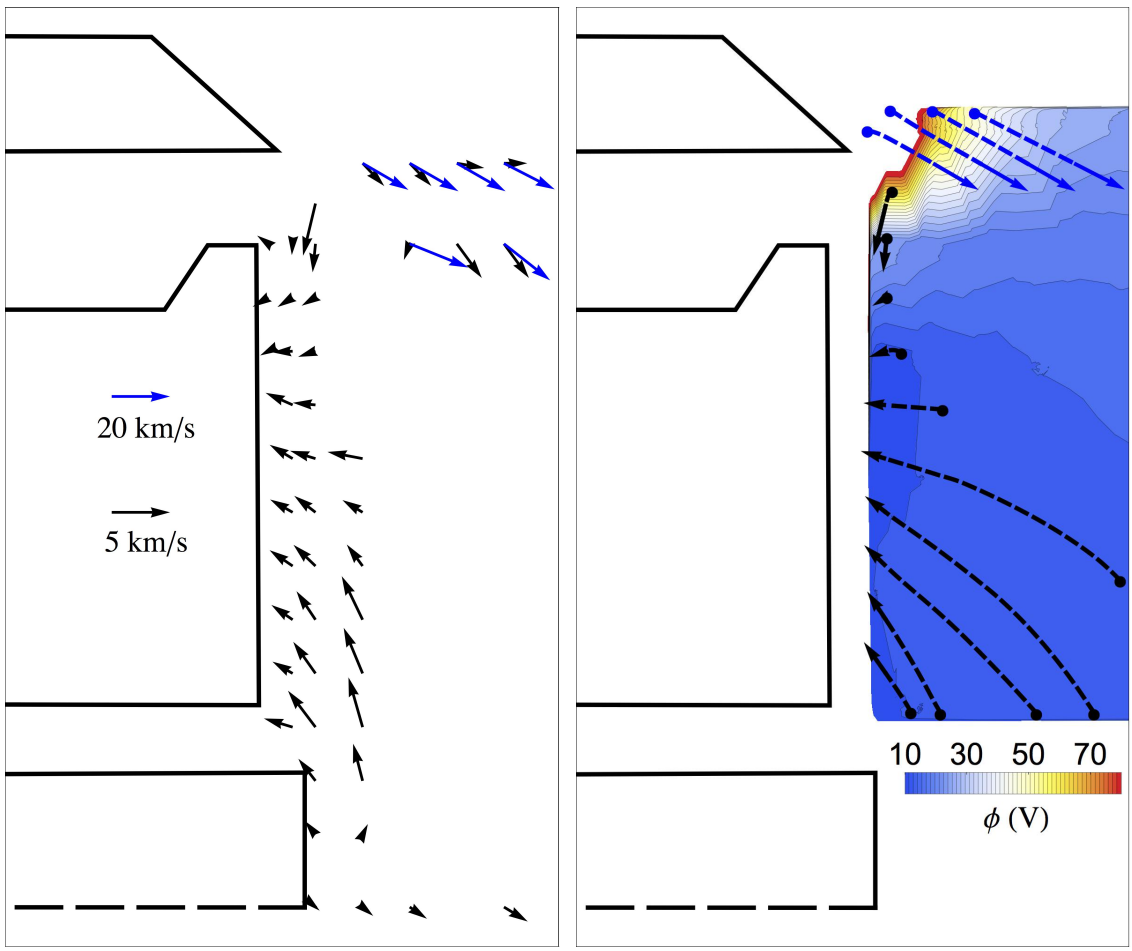

(a) (b)

Figure 7: a) Vector field in the region adjacent to the inner pole. Blue vectors denote beam ions with high kinetic energy directed downstream, and black vectors denote low energy plume ions originating near the inner pole and cathode. The scaling factor for the blue ions is four times larger than the black ions. b) Plasma potential measurements in the near plume with superimposed ion trajectories.

The nature and origin of these two populations can be understood in the context of the local plasma properties. Fig. 7(b) shows measurements of the plasma potential with respect to ground, ϕ, in the near-field pole region that we mapped with the probing scheme described in Sec. II.B. Near the cathode and radially inward from the channel, the potential gradients in the region adjacent to the pole are low. With

increasing radius, the edge of the plasma beam is marked by a rapid potential increase. We use this data to show the origins of the ions explicitly by assuming electrostatic acceleration and solving the governing equation, $d^2\vec{r}/d^2t = -q/m_i\nabla\phi$. We use initial conditions for the position and velocity vectors from both the blue and black populations and numerically integrate this equation backward in time. The integration stops when a trajectory either leaves the domain or when the kinetic energy of the population decreases below $E = 1$ eV. The results from the integration are shown in Fig. 7(b) as dotted lines terminating in circles. The blue-labeled trajectories clearly indicate the origin of the high velocity species: the population is born in the channel and passes through the 300 V acceleration zone (equivalent to $\sim$ 20km/s). These high energy ions thus are members of the beam population that contributes to thrust. The black-labeled population, on the other hand, originates in the near-field region characterized by low plasma potential. The ions born here are the products of charge-exchange collisions and ionization from the cathode plume. The slight potential drop from their starting locations to the poles provides sufficient impetus to direct them back toward the thruster face. However, the change in potential is small, 2 - 10 V, which explains why their kinetic energy at the pole is low.

B. Ion temperature at the poles

We show in Fig. 8 IVDFs from the East and West beam directions at a location 3 mm downstream of the inner edge of the pole. These plots demonstrate that although the average ion velocity is < 2 km/s in this region, there is a non-negligible fraction of the ion population in both directions with speed exceeding 5 km/s. The shapes in Fig. 8 also suggest that the distributions along both directions are thermalized. We therefore can assign an effective ion temperature to each distribution, T_i, by applying a Maxwellian fit: $f_i = A\exp[-m_i\left(v - v_d\right)^2/2T_i] + c$ where v_d denotes the drift velocity, A is a constant, and c is an offset that accounts for the noise floor. Best fits are shown for both directions with corresponding values of $T_i = 10.4$ and 13.4 eV for the West and East directions respectively. The close proximity of these temperatures indicates that velocity dispersion is approximately isotropic in both directions.

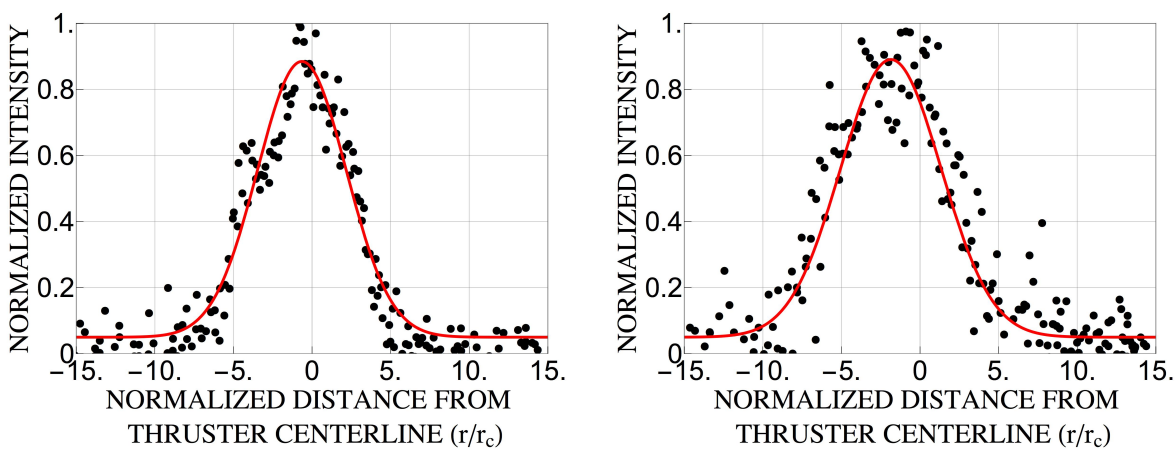

(a) (b)

Figure 8: Measured IVDFs along the West (a) and East (b) directions at a location 3 mm downstream of the inner edge of the inner pole. Maxwellian fits to the measurements (red) yield ion temperatures of $T_i = 10.4$ eV and 13.4 eV.

The Maxwellian shape and isotropy persist for all the measurements of the IVDF at the closest downstream location from the pole (the first column on the left in Fig. 7(a)). This is illustrated by Fig. 9 where we have used Maxwellian fits to each beam direction to plot the measured temperatures as a function of radial position in Fig. 9. We also show the average value of the ion temperature at each point. The small discrepancy between the value from each beam direction compared to the average confirms the approximate isotropy of the velocity dispersion. Fig. 9 also shows that the values of temperature, $T_i = 4.2 - 12$ eV, greatly exceed classical expectations, i.e. $T_i \gg T_n \approx 0.1$ eV where T_n is the neutral temperature. These high temperatures and their corresponding spread in velocity space are real in so much as they cannot be explained by the other dominant broadening effect in this region, the Zeeman effect. Indeed, referring to our discussion in

Sec. II.D, we have found for the measured magnetic field in this region, the Zeeman effect from Eq. 2 for all cases with $r < 0.6r_c$ introduces an error less than 15% of our measured measured values. The one exception is the data point at $r = 0.62r_c$ at the edge of the pole, where the Zeeman effect yields a larger uncertainty of 30%. These percentage errors show that while the Zeeman spread can lead to a finite overestimate in the ion temperature, the small scale rules out the the Zeeman broadening as the dominant contributor to the measured ~ 10 eV values. Uncovering the mechanism leading to the high effective temperature is beyond the scope of this investigation, but a likely candidate is that these IVDFs are the time-averaged result of the strong, low frequency ionization-like oscillations that have been measured in this region.[36]

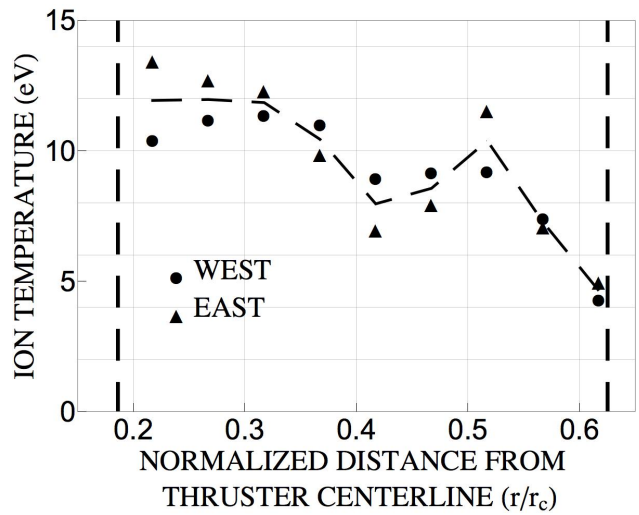

Figure 9: Ion temperature along each beam direction at the inner pole. The dashed line denotes the average of both both beam directions.

Regardless of the mechanism, the wide dispersion in velocity space indicated by the measurements at the pole has direct implications for pole erosion. Indeed, even though the average kinetic energy for the ions fluxing to the poles is low, as we will see in the next section, the ion energies in the wings of the IVDF can have a disproportionally high impact on sputtering.

C. Erosion estimates from ions impacting pole

We calculate in this section the wear that would result if the fluxing ion populations shown in Fig. 7 were incident on a strip of test molybdenum mounted on the inner pole. We consider molybdenum instead of the actual pole material, iron, in order to have a direct comparison with the results from Sekerak et al who employed molybdenum coupons in their wear test of the H6MS inner poles.[6] The erosion from the incident ions on this molybdenum is estimated in two ways: first by considering the average properties and then by integrating over the incident distributions. The former approach provides a first order assessment of whether or not the average kinetic energy of the impacting particles is sufficiently high to explain the erosion, and the latter approach takes into account the high dispersion of the ion distribution.

For estimating the erosion using the average flux properties, we treat the ions as monoenergetic. The expression for the erosion rate at the pole in this case is given by

$$\epsilon_t = 3.6 \times 10^9 \gamma \left(\theta_{(p)}, E_{(p)}\right) \Phi_{(p)i} m_t / \rho_t, \tag{3}$$

where (p) denotes the quantity at the pole, m_t is the mass of a molybdenum atom in kg, ρ_t is the density of Molybdenum in kg/m^3, Φ_i is the ion flux density to the surface in ion/m^2/s, ands γ is the sputtering yield, which is a function of the angle of incidence and the kinetic energy (Appendix). We can evaluate Eq. 3 to find the effective erosion rate provided we know the average ion flux, angle of incidence, and average kinetic energy of the ions at the pole. However, due to limited accessibility and low signal to noise in this region, the closest direct measurements we could make were 3 mm downstream of the surface. It is possible to translate this downstream data to a direct evaluation of Eq. 3 if we make the approximation that that the measurement domain is at the edge of a collisionless thin sheath. In this case, the flux at pole, $\Phi_{(p)i}$ is

the same as that measured downstream of the poles Φ_i; the kinetic energy at the pole, E_p is related to the average kinetic at the measurement location, E, by $E_p = \phi + E$; and the angle of incidence at the pole is

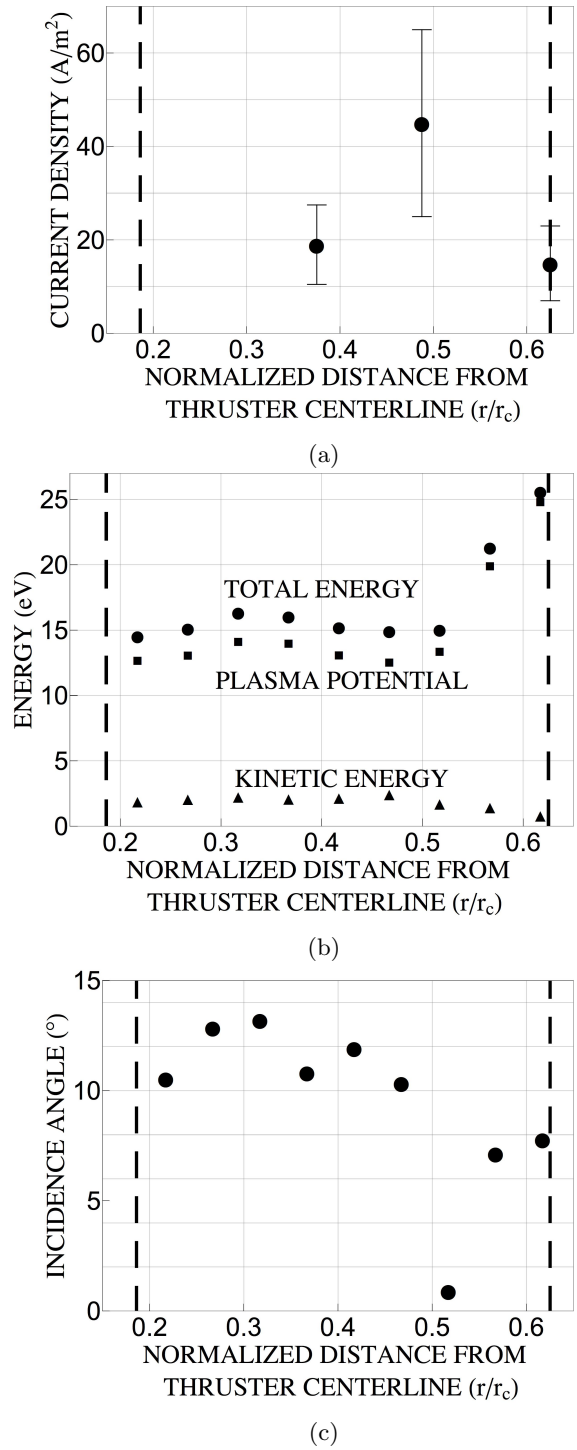

Figure 10: (a) Ion current density to the inner pole as a function of radial distance from centerline. (b) Average angle of incidence for ions after transiting the sheath. (c) Total energy at the pole face, plasma potential at sheath, and kinetic energy of ions at the sheath. The dashed lines denote the edges of the inner pole.

altered by the fall through the sheath:

$$\theta = \tan^{-1}\left[\frac{v_y}{\left(\frac{2\phi}{m_i} + v_x^2\right)^{1/2}}\right], \tag{4}$$

where v_x and v_y denote components of the ion velocity in the axial and radial directions respectively.

With these relations in mind, we measured the average ion population parameters in the following way. For the ion flux density, we assumed singly charged ions were the dominant species at the poles and related the Faraday probe measurements of current density to the flux with $\Phi_i = j_i/q$. Fig. 10(a) shows the measured ion current density as a function of radial position, which yielded the average value of $j_i = 26.3 \pm 21$ A/m^2 that we employed for this study. For the total energy at the pole, E_p, we calculated the average kinetic at the sheath, E, from the bulk flow velocity vectors (first column in Fig. 7(a)) and added the plasma potential measured at the same location, $E_p = E + \phi$. Fig. 10(b) shows E_p plotted with ϕ and E and illustrates how the majority of the ion energy was gained from the plasma potential drop to the pole. For the incidence angle, we extracted the average velocity vectors from the LIF measurements to evaluate Eq. 4 as a function of radial position on the pole. Fig. 10(c) shows θ as a function of position, which is is close to normal, $\theta = 0°$ in all cases. This is expected given that the kinetic energy for ions entering the sheath is only from 1-3 eV and the sheath drop is $10 - 15$ V. The sheath drop thus redirects the incident flux to the normal.

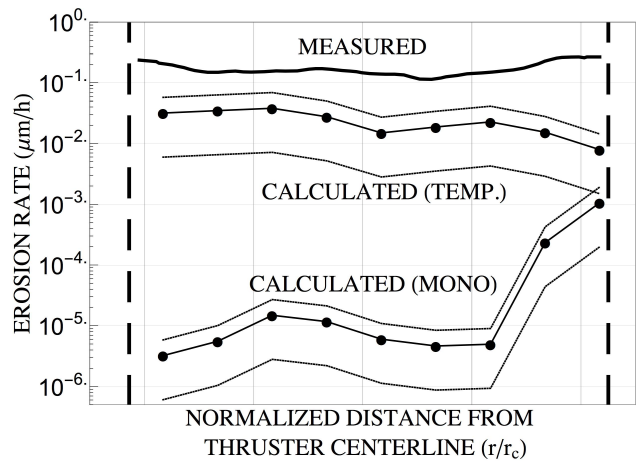

Figure 11: Calculated erosion rate on molybdenum assuming monoenergetic incident ions. The dotted bars indicate uncertainty due to variance in flux measurements and the sputtering model. Results are compared with measured erosion from Ref. 6.

Using the plasma measurements from Fig. 10, we evaluate Eq. 3 and plot the result as a function of radial position in Fig. 11. The upper and lower bounds on the curve reflect the error in the flux measurements. For comparison, we show the erosion measurements from Sekerak et al[6] for the direct wear test performed on molybdenum under the same operating conditions. We draw two major conclusions from Fig. 11. First, the trends of the calculated curve for erosion mirror the trends in plasma potential (Fig. 10 (c)). This is because the potential drop through the sheath is the dominant mechanism for imparting energy to the ions. Second, it is evident from Fig. 11 that the estimates for erosion based on the bulk flow properties of the plasma are 2 to 4 orders of magnitude too low to explain the rates measured by Sekerak et al. This discrepancy can be understood in the context of Ref. 6 (Table 8) and Ref. 8 (Sec. 5.A) which showed that for current densities comparable to what we observe at the poles $j_i \sim 20$ A/m^2, the necessary energy of monoenergetic ions would have to be approximately 75-150 eV in order to yield the observed erosion profiles. Our low kinetic energy of ions entering the sheath (1-3 eV) coupled with the small sheath drop $10 - 25$ V are insufficient to provide this energy level.

While our inability to capture the erosion with average flux measurements from the data at first appears paradoxical, part of the difference between the calculated erosion and the measured results can be attributed

to the simplifying assumption that the incident ions are monoenegetic. In reality, the ion distribution function exhibits a significant dispersion in velocity space with higher energy ions than the mean. Since the ion sputtering yield (Appendix, Eq. 9) has a highly nonlinear dependence on ion energy, even a small fraction of ions at higher energy can contribute to larger erosion erosions. To take this possibility into consideration, we assume again that we can treat the measurement locations as the edge of a thin sheath to the poles. This allows us to re-write Eq. 3 as an integral over the velocity distribution function at the measurement location:

$$\epsilon_t = 3.6 \times 10^9 \left(\frac{m_t}{\rho_t}\right)\left(\frac{j_i}{q\langle v_x\rangle}\right)\int_{-\infty}^{0}\int_{-\infty}^{\infty}\gamma\left(E+q\phi,\theta\right)v_x f_i\left(v_x,v_y\right)dv_y dv_x, \tag{5}$$

where $E = 1/2m_i\left[v_x^2+v_y^2\right]$ is the energy of ions entering the sheath, ϕ is the plasma potential at the sheath edge, θ is given by Eq. 4, and f_i is the ion velocity distribution function at the measurement point. We have made the explicit substitution for the flux $\Phi_i\left(v_x\right) = v_x(j_i/\left(q\langle v_x\rangle\right)$ where $\langle v_x\rangle = \int_{-\infty}^{0}\int_{-\infty}^{\infty} v_x\left(v_x\right)f_i\left(v_x,v_y\right)dv_y dv_x$.

We do not have an explicit form for $f_i\left(v_x,v_y\right)$ as our LIF measurements only yielded projections of the distribution function onto the two orthogonal axes that we interrogated with the beams. However, since the observations from Sec. III.B showed the IVDFs along the pole are thermalized and isotropic, we can approximate the ion distribution function in two dimension as

$$f_i\left(v_x,v_y\right) = \left(\frac{m_i}{2\pi T_i}\right)e^{-\frac{m_i}{2T_i}\left(v_x-v_{d(x)}\right)^2}e^{-\frac{m_i}{2T_i}\left(v_y-v_{d(y)}\right)^2}, \tag{6}$$

where the ion temperature at each radial location is given by the average value indicated in Fig. 9 and the average drift velocities $v_{d(x)}, v_{d(y)}$ are given by the measurements in Fig. 7(a). Armed with this result, we use the average value for j_i from Fig. 10(a) and integrate over Eq. 5 to find in Fig. 11 estimates for the erosion that take into consideration the velocity dispersion. It immediately can be seen from this plot that the magnitude of the erosion is 2-4 orders of magnitude higher than the calculated erosion that assumes monoenergetic ions. This increase results from the energetic ions in the wings of the ion distribution that have orders of magnitude higher sputtering yields (Appendix, Eq. 9). Significantly, at the outer edge of the pole, the estimates for erosion from the thermal spread estimates and the monoenergetic beam assumption start to converge. This occurs because the ion temperature as measured with the LIF is lower at this point $T_i = 4.5$ eV such that the the beam appears more monoenergetic. Despite the fact that including the velocity dispersion does increase the calculated erosion, however, we ultimately find from Fig. 11 that we still underestimate the measured sputtering rate by a factor of eight. This suggests that even allowing for the thermal spread—which ultimately is an overestimate given the effect of Zeeman splitting—the observed erosion cannot be captured. Examined in the context of Refs. 8 and 6 this result is consistent with the assertion that for our measured flux levels, it would require a monoenergetic beam with ∼75 eV to explain the observed erosion rates. In our case, only the very extremes wings of the IVDFS allow for this level of energy.

In summary, we have shown through direct physical measurements that steady-state estimates of the bulk properties in the plasma do not yield sufficiently high ion energy of flux to explain the observed erosion. We explore in the next section a possible resolution to this contradiction.

IV. Discussion

The results from Fig. 11 demonstrate how the observed ion energies and flux at the sheath are insufficient to explain the observed erosion rates. One of the major limitations for the LIF measurements at the pole, however, is the low signal to noise ratio. This is a consequence of the sparseness of the plasma and low electron temperature in this region—both of which lower the population of the metastable state targeted by the LIF scheme. It is possible then that although the LIF IVDFs describe the bulk distribution of plume-born ions in the region, there may be a small population of higher energy ions originating from near the channel (greater than 70 V potential contour in Fig. 7(b)) that are obscured in the wings of the IVDF by the high noise. Indeed, even a low density of such ions fluxing to pole compared to the plume ions may be sufficient to explain the erosion provided they have sufficiently high energy. This is because of the highly nonlinear nature of the sputtering yield (Eq. 9 in the Appendix). To illustrate how this could be the case, we use Eq. 3 for a mono-energetic beam and the experimental results for erosion rate from Sekerak et. al (Fig. 11) to determine the density of a beam of high energy ions at the sheath edge, n_b, that would be sufficient to

explain the erosion. We assume obliquely incident ions, $\theta = 45°$, at the sheath with fixed kinetic energy E and temperature $T_i = 1.0$ eV. These assumptions are consistent with the notion of ions born in the beam's potential and falling back to the pole. The temperature we assume is based on previous measurements of the spread of ion distribution function in a thruster plume for a thruster at the same power level.[31]

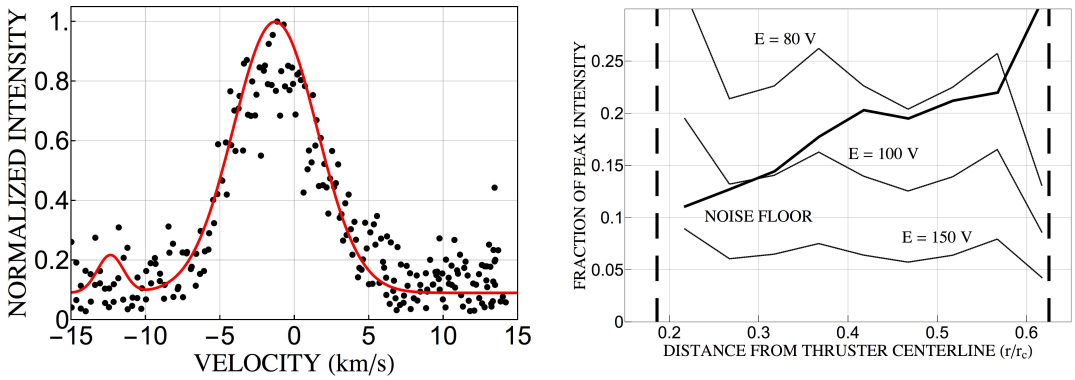

(a) (b)

Figure 12: (a) The ideal LIF measurement (red) in the absence of noise along the West injection beam for the ion distribution function that includes the bulk population and a high energy beam with sufficient density to cause the measured erosion. The data from the LIF measurement at this location is also shown. (b) Intensity of the LIF signal corresponding to a population density of beam ions with sufficient energy, E, to cause the measured erosion profiles. This intensity is expressed as a fraction of the peak intensity measured for the slow, bulk population. The measured noise floor for the LIF is also shown.

With these assumptions in mind, we find that at the normalized pole position $r = 0.5r_c$ for an ion energy beam with $E = 100$ V, the beam density at the sheath necessary to explain the observed erosion is $n_b = 0.036n_0$ where n_0 denotes the density of the bulk, slow moving population of ions from the near field plume. We plot in Fig. 12(a) the ion distribution that would result if this 100 V energetic beam were superimposed on the bulk particle distribution we measured at this location. We also show the data from the actual LIF measurement for the distribution function at this position. This figure serves to demonstrate how the low signal to noise in this region precludes our ability to resolve the presence of such a high energy beam population.

We generalize this assessment by considering that the peak intensity of an LIF signal corresponding to a beam of density n_b with temperature $T_{i(b)}$ would scale as $P_b = \alpha n_{i(b)}(T_{i(b)})^{-1/2}$ where α is a constant. In contrast, the intensity of the LIF at the peak of the bulk, low energy population is given by $P_0 = \alpha n_{i(0)}(T_{i(0)})^{-1/2}$. The ratio of the beam intensity signal compared to the bulk signal is thus

$$\eta = \frac{n_b}{n_i}\left(\frac{T_{i(b)}}{T_{i(0)}}\right)^{1/2}. \tag{7}$$

We plot this parameter as a function of radial position for three different values of kinetic energy in Fig. 12(b). For comparison we show the signal to noise ratio for the LIF traces as a function of radius at the pole as well. This plot demonstrates that for ion energies above 100 eV, the requisite density of the population necessary to explain the erosion could be obscured by the noise in the signal. It thus is possible that high energy ions do in fact exist at the poles, but we could not resolve them with the current diagnostic's sensitivity.

The location of the plasma in the H6MS supports this mechanism. We show in Fig. 13(a) the measured axial component of the ion velocity along channel centerline as a function of normalized distance from the thruster exit plane. It is evident from this plot that the the acceleration zone in the H6MS thruster is displaced downstream of the discharge chamber exit and the inner pole. This downstream shift is the direct result of the magnetic shielding topography[3] and has the consequence that the plasma potential is high downstream of the exit plane. Indeed, we illustrate this qualitatively by neglecting ionization and relating the axial component of velocity to plasma potential through the approximate relationl: $\phi = 300 - 1/2 m_i v^2/q$.

Plotting this effective plasma potential in Fig. 13(b) demonstrates how the potential only begins to decrease with position downstream of the pole.

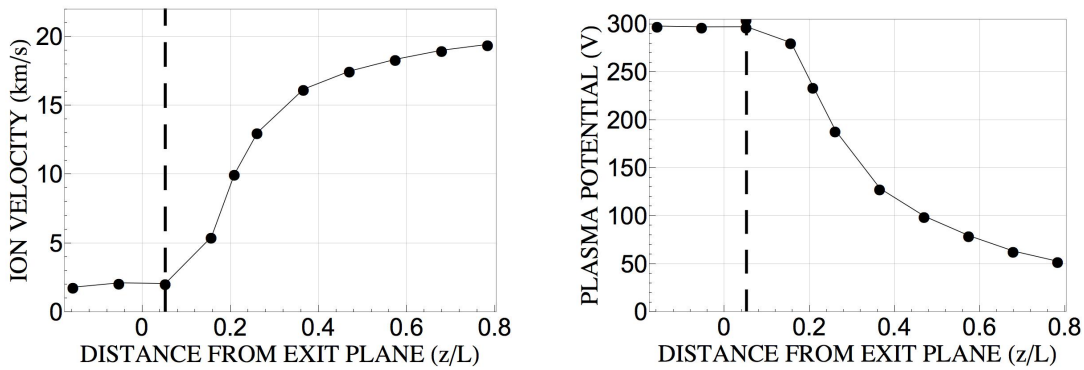

(a) (b)

Figure 13: (a) LIF measurement of the axial component of the ion velocity at channel centerline as a function of distance from the thruster exit plane. (b) Plasma potential on centerline inferred from the axial velocity measurements. The dotted line in both cases denotes the axial location of the thruster inner pole.

The implication of this displacement in potential is that ions born downstream of the exit plane at high values ($\phi > 150$ V) have a path back to the pole. We illustrate empirically how this type of trajectory is possible by again assuming electrostatic acceleration (as we did in Fig. 7(b)) and using our measured plasma potentials to integrate ion motion. It was necessary in this case to extrapolate the plasma potential measurements to the poles as our probes did not interrogate the 3 mm gap downstream of this surface. For initial conditions with the ions at rest at the edge of the beam near the thruster exit plane, we show in Fig. 14(a) numerically integrated trajectories that demonstrate how ions born at $\phi \approx 90$ V at the edge of the beam can be electrostatically accelerated to the poles. We similarly show in Fig. 14(b) the kinetic energy with which the ions following these trajectories impact the poles after falling through the sheath. These energies are a factor of 5-6 higher than the the energy of the bulk of the population of the ions that we measured with the LIF in Fig. 10(b). In light of these results, there thus is reason to believe that there may be a small population of energetic beam ions impacting the pole.

As we showed in Fig. 12, however, even if a small population of energetic ions does follow the trajectories illustrated in Fig. 14(a), the low signal to noise ratio of the LIF measurements may prevent us from measuring them. Faced with this limitation, we turn to JPL's Hall thruster code, Hall2De,[37] to make a first order determination as to whether or not these energetic ions should exist at the pole. Hall2De is a multi-fluid, hybrid solver that treats the electrons as a single fluid and models the ions as a combination of fluids or particles that are grouped according to charge state and where they are born in the plasma. The ion populations interact through collisions and ionization events. In order to compare to our LIF measurements, we have employed for our simulation three ion species that mirror the populations we observed experimentally in Fig. 7(a): a fluid population for ions born in the region of the cathode, a fluid population for ions born in the main beam in the discharge chamber, and particle-in-cell (PIC) treatment for ions born in the plume. The demarcator for the PIC ions is based off a contour of constant plasma potential, which in this case is chosen to be 250 V. We note here that Hall2De has been employed in an previous attempt to examine pole erosion in the H6MS;[8] however it was found in this work that the estimates for ion energy at the poles were too low to explain the observed wear rates. The version of Hall2De we use for this study is different from the one in Ref. 8 in that it has a refined models for the physical interactions at the cathode[38] and the cutoff potential for the plume species is 250 V versus 75 V in the previous study. The Hall2De output we use has been validated against experimental measurements by matching the measured performance characteristics of the thruster at 300 V and 20 A as well as the measured LIF measurement of the axial component of the ion velocity (Fig. 13(a)) and the plasma potential in the near field region (Fig. 7(b)).

With this in mind, we have used the PIC module for Hall2De to generate an ion energy distribution function (IEDF) for ions fluxing toward the poles. We show in Fig. 15(a) the simulated IEDF at the center of the inner pole and 3 mm downstream of its surface. This result, depicted on a log-linear scale, shows two

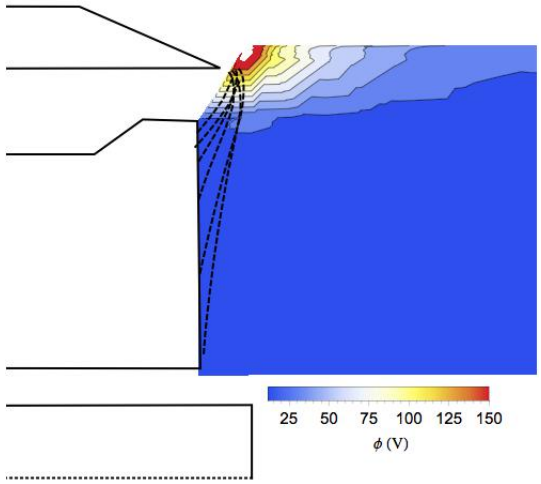

(a)

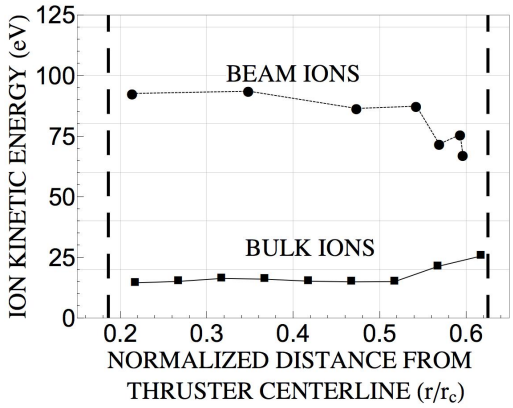

(b)

Figure 14: (a) Trajectories for ions to the pole assuming they are born at rest at the beam edge. (b) Kinetic energy of these ions impacting the poles contrasted with the average kinetic energy of the bulk distribution of the population fluxing to the pole.

prominent features. The first is a low energy peak which corresponds to the PIC ions born in the near-field region where the plasma potential is low. The second is the population of ions with energies ranging from 100-200 eV. This feature, comprising just 10% of the total distribution function, is confirmation that the mechanism shown qualitatively in Eq. 14(b) is plausible: ions born at high potential in the plume can be accelerated back to the pole at high energy. Moreover, by comparing this IEDF from the PIC ions with our measured LIF energy distribution from the West beam at this same physical location in Fig. 15(b), we can see that our suppositions outlined in Fig. 12 are also confirmed. In particular, the LIF signal is sufficiently strong to resolve the lower energy, bulk ion population, but the high energy population density is too sparse to be distinguished from the noise. As an aside, we note that the discrepancy between the peak in the measured energies from PIC and the ones we report from our electrostatic integration in Eq. 14(b) can be explained by the fact that our measurements of the plasma potential only extend to regions where $\phi = 120$ V. The simulations from Hall2De, however, capture the whole channel and therefore ions born at even higher potentials can fall back to the poles.

Fig. 15 thus provides quantitative evidence—informed by validated modeling at this experimental condition—that there are energetic ions fluxing back to the poles from the plasma. We can expand upon this result by using the code outputs to to determine if this high energy population is sufficiently dense to explain the

observed erosion in this region. With this in mind, we note that the simulated flux of the PIC ions at the modeled location is 10 A/m^2, which is within the error bars from our measured flux. Using this value and the same integration technique we applied for Eq. 5, we assume an oblique angle of incidence at 45 degrees to calculate the predicted erosion rate with Hall2de at this pole location (Table 1). We similarly show in this table the predicted erosion from Hall2De if we exclude the high-energy ions, the calculated rates based on LIF measurements assuming monoenergetic ions and ions with dispersion, and the measured rate from Sekerak et al.[6] As we can see, the PIC simulation captures within a factor of two the measured erosion at the poles, but it only does this if the high energy ions from the high potential are included. Interestingly, the calculated erosion including ion temperature exceeds the PIC simulation where the high energy ion tail has been neglected. This suggests that the simulation results in this region underpredict the effective thermal spread in the bulk distribution. The reason for this is not known but one possibility is that the model does not correctly capture the potential fluctuations we alluded to in Sec. III that might explain the observed thermal spreading.

Table 1: Erosion rates in μh/hr at the center of inner pole ($r = 0.37r_c$)

Measured	PIC	PIC (no high energy)	LIF (monoenergetic)	LIF (with temp.)
1.4 $\times 10^{-1}$	1.1 $\times 10^{-1}$	2.2 $\times 10^{-3}$	5.9 $\times 10^{-5}$	1.4 $\times 10^{-2}$

In summary, the simulated results support the conclusion that the erosion at the poles cannot be solely explained by the bulk flow of the ion population. Indeed, the reason why our calculated erosion rates underpredict the erosion stems from the fact that the LIF measurements cannot resolve a small population of high energies born downstream of the pole and at high potential that fall back to the pole. This wear mechanism is possible in the magnetically shielded thruster because the acceleration zone is shifted downstream by the magnetic field topography.

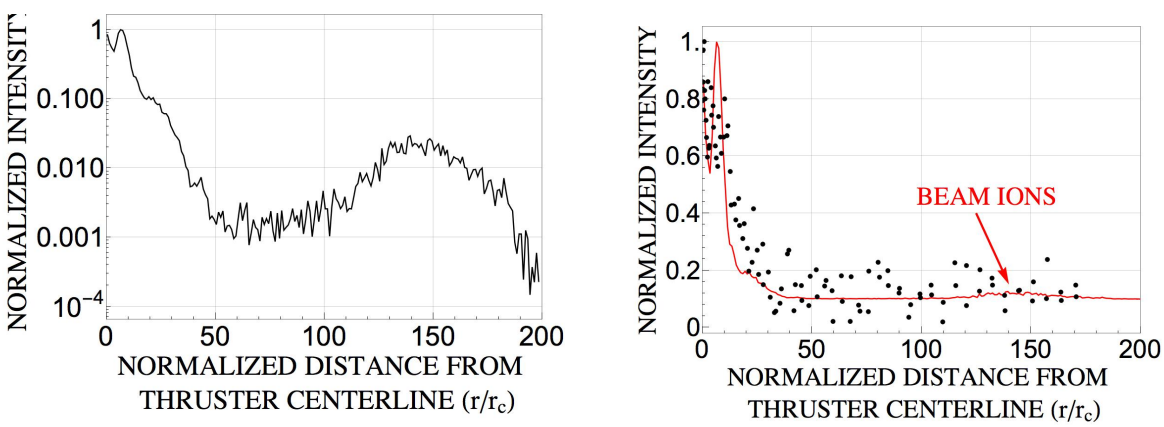

(a) (b)

Figure 15: (a) Log-linear plot of ion energy distribution function from Hall2De PIC simulations at the center of the inner pole and 3 mm downstream. (b) Comparison between the PIC distribution function and the measured distribution function with LIF at the same location. The population of the ion energies is also indicated.

V. Conclusion

This study was motivated by a need to understand anomalous erosion that previously had been observed at the inner magnetic pole of the H6MS 6-kW magnetically shielded thruster. We have directly characterized the plasma in this region through a combination of laser induced fluorescence measurements and a set of spatially-resolved and surfaced mounted plasma probes. Our measurements revealed that the bulk population

of ions fluxing to the poles was dominated by a low energy species ions born in the region immediately adjacent to the pole and accelerated to the pole by gradual potential gradients. The effective temperature of these ions was high $T_i \approx 10$ eV— a result which we have postulated may be related to low-frequency high amplitude plasma oscillations in the near field region. We ultimately found that even allowing for this high spread in velocity, the energy of the incident ions for the bulk population yielded a calculated erosion rate approximately 8 times lower than the measured wear rate.

In light of this result, we have examined the possibility that another, undetected mechanism apart from the incident bulk population of ions may be responsible for the erosion. In particular, since the magnetic shielding topography of the H6MS shifts the acceleration region downstream from the inner pole of the thruster, it is possible that ions born at the high potential near the beam edge will fall back to the grounded pole surface with a high kinetic energy. Since the sputtering yield is highly nonlinear, even a small population of these ions (compared to the bulk, plume born ions) that reaches the pole may be sufficient to explain the observed erosion rates. With this wear mechanism in mind, we have used experimental measurements of the plasma potential in the near field to demonstrate that there is an electrostatic path for ions born at the edge of the plasma beam to fall back to the cathode with energies exceeding 90 eV. Moreover, by implementing a validated model of the thruster in this region, we have shown that the expected density of these energetic ions at this inner pole (10% of the bulk distribution) is sufficient to explain the measured erosion within a factor of two. This density is too low, on the other hand, to yield an LIF signal that could be distinguished from the noise floor, which would explain why we did not detect such a high energy population in our measurements. Taken in the context of our experimental measurements, this simulated result from a validated model thus strong evidence that the erosion at the poles may be attributed to this high energy population.

In summary, we have used a combination of experiment and theory to deduce that a probable cause for the erosion of the pole face in the H6MS is that the magnetic shielding pushes the plasma sufficiently far downstream that high energy ions have a path to return to the poles. This mechanism was originally proposed by Mikellides in Ref. 7 though not substantiated by modeling and experiment until now. The implication of this result is that unshielded Hall thrusters that contain their acceleration zone well within the thruster channel likely will not exhibit this type of erosion. And indeed, in the decade that the H6US, the unshielded variation of the H6MS, has been investigated, the erosion at the poles has not been reported as a potential issue. Of course, as noted in Ref. 6, the reductions in discharge chamber erosion that can be achieved with magnetic shielding far outstrip the relatively slow increase in erosion rates incurred at the poles. For long duration missions, pole erosion may still pose a problem, however, and with this in mind, the conclusions of our study open the possibility of examining mitigation techniques. In particular, the most readily apparent path forward is to explore methods to eliminate the path from the high potential region to the poles. Improved modeling results validated by the experimental measurements ultimately may help guide this effort.

Acknowledgments

The research described in this paper was carried out at the Jet Propulsion Laboratory, California Institute of Technology, under a contract with the National Aeronautics and Space Administration and funded through the Advanced In-Space Propulsion Technologies program. The authors would like to acknowledge Ray Swindlehurst and Nowell Niblitt for their assistance in running the experimental facility.

Appendix

While there are a number of models for both the angular and energy dependence of the sputtering, we adopt here the form for angular sputtering per Yamamaru[39] that was employed by Lopez-Ortega et al[8] in their previous numerical study of pole erosion:

$$\gamma_\theta(\theta) = \cos(\theta)^{-c_0} \exp\left[-c_1\left(\cos(\theta)^{-c_2} - 1\right)\right], \tag{8}$$

where for molybdenum, $c_0 = 2.5204, c_1 = 0.8552$, and $c_2 = 1$. This form indicates that preferential scattering occurs at oblique angles. For the energy dependence of sputtering, we employ the semi-empirical fit implemented by Sekerak et. al[6] in their experimental wear test for pole erosion

$$\gamma_E(E) = s_n^{KrC}(\epsilon)\left[\beta - \left(\frac{E_{th}}{E}\right)^{\eta}\right], \tag{9}$$

where β, γ, and E_{th} are all fit parameters. The leading term s^{KrC} is the Kr-C potential given by

$$s_n^{KrC}(\epsilon) = \frac{0.5\ln(1+1.2288\epsilon)}{\epsilon + 0.1728\sqrt{\epsilon} + 0.008\epsilon^{0.1504}} \tag{10}$$

with the reduced energy

$$\epsilon = E\frac{M_2}{M_1+M_2}\frac{a_L}{Z_1 Z_2 e^2}. \tag{11}$$

Here Z_1 is the atomic number of xenon, Z_2 is the atomic number of Molybdenum, $e^2 = 14.4\text{eV}\mathring{A}$, and the Lindhard screening length is given by

$$a_L = 0.4685\left(Z_1^{2/3} + Z_2^{2/3}\right)^{-1/2}\mathring{A}. \tag{12}$$

The best-fit parameters for Eq. 9 we use are $E_{th} = 120$, $\eta = 1.15$, and $\beta = 1.0$.[6]

References

[1]De Grys, K., Mathers, A., and Welander, B., "Demonstration of 10,400 Hours of Operation on a 4.5 kW Qualification Model Hall Thruster," *46th Joint Propulsion Conference and Exhibit, July 25-28, 2010. Nashville, TN. AIAA-2010-6698*.

[2]Mikellides, I. G., Katz, I., Hofer, R. R., and Goebel, D. M., "Magnetic shielding of walls from the unmagnetized ion beam in a Hall thruster," *Applied Physics Letters*, Vol. 102, No. 2, 2013.

[3]Mikellides, I. G., Katz, I., Hofer, R. R., and Goebel, D. M., "Magnetic shielding of a laboratory Hall thruster. I. Theory and validation," *Journal of Applied Physics*, Vol. 115, No. 4, Jan. 2014, pp. 043303.

[4]Hofer, R. R., Goebel, D. M., Mikellides, I. G., and Katz, I., "Magnetic shielding of a laboratory Hall thruster. II. Experiments," *Journal of Applied Physics*, Vol. 115, No. 4, 2014, pp. –.

[5]Goebel, D., Jorns, B., Hofer, R., Mikellides, I., and Katz, I., "Pole-piece Interactions with the Plasma in a Magnetically Shielded Hall Thruster," *50th AIAA/ASME/SAE/ASEE Joint Propulsion Conference and Exhibit, Cleveland, OH, July 28-30, 2014. AIAA-2014-3899.*, 2014.

[6]Sekerak, M., Hofer, R., Polk, J., Jorns, B., and Mikellides, I., "Wear Testing of Magnetically Shielded Hall Thruster at 2000 s Specific Impulse," *34th International Electric Propulsion Conference, Hyogo-Kobe, Japan, July 6-10, 2015. IEPC-2015-155*, 2015.

[7]Mikellides, I. G., Ortega, A. L., and Jorns, B., "Assessment of Pole Erosion in a Magnetically Shielded Hall Thruster," *50th AIAA/ASME/SAE/ASEE Joint Propulsion Conference and Exhibit, July 28-30, 2014, Cleveland, OH. AIAA-2014-3879.*.

[8]Ortega, A., Mikellides, I., and Katz, I., "Hall2De Numerical Simulations for the Assessment of Pole Erosion in a Magnetically Shielded Hall Thruster," *34th International Electric Propulsion Conference, Hyogo-Kobe, Japan, July 6-10, 2015. IEPC-2015-249.*.

[9]Brophy, J., Friedman, L., Culick, F., et al., "Asteroid Retrieval Feasibility Study," *Keck Institute for Space Studies, Califonia Institute of Technology, Jet Propulsion Laboratory*, 2012.

[10]Hofer, R. Kamhawi, H. H. D. e. a., "Development Approach and Status of the 12.5 kW HERMeS Hall Thruster for the Solar Electric Propulsion TechnologyDemonstration Mission," *34th International Electric Propulsion Conference, Hyogo-Kobe, Japan, July 6-10, 2015. IEPC-2015-186.*.

[11]Hofer, R., Jorns, B., Polk, J., Mikellides, I., and Snyder, J., "Wear test of a magnetically shielded Hall thruster at 3000 seconds specific impulse," *33rd International Electric Propulsion Conference, Washington, D.C., Oct. 6-10, 2013. IEPC-2013-033*.

[12]Haas, J. M., Hofer, R. R., Brown, D. L., Reid, B. M., and Gallimore, A. D., "Design of the H6 Hall Thruster for High Thrust/Power Investigation," *54th JANNAF Propulsion Meeting, Denver, CO, May 14-17, 2007*, 2007.

[13]Brown, D., Reid, B., Gallimore, A., Hofer, R., Haas, J., and Larson, C., "Performance Characterization and Design Verification of the H6 Laboratory Model Hall Thruster," *54th JANNAF Propulsion Meeting, Denver, CO, May 14-17, 2007*, 2007.

[14]Reid, B., Gallimore, A., Hofer, R., Li, Y., and Haas, J., "Anode Design and Verification for the H6 Hall Thruster," *54th JANNAF Propulsion Meeting, Denver, CO, May 14-17, 2007*, 2007.

[15]Hofer, R., Goebel, D., and Watkins, R., "Compact LaB6 Hollow Cathode for a 6 kW Laboratory Hall Thruster," *54th JANNAF Propulsion Meeting, Denver, CO, May 14-17, 2007*, 2007.

[16]Huang, W., Gallimore, A., and Hofer, R., "Neutral Flow Evolution in a 6-kW Hall Thruster," *Journal of Propulsion and Power*, Vol. 27, 2011, pp. 553–563.

[17]Goebel, D., Jameson, K., and Hofer, R., "Hall Thruster Cathode Flow Impact on Coupling Voltage and Cathode Life," *Journal of Propulsion and Power*, Vol. 28, 2012, pp. 355–363.

[18]Goebel, D. M. and Watkins, R. M., "Compact lanthanum hexaboride hollow cathode," *Review of Scientific Instruments*, Vol. 81, No. 8, 2010.

[19]Jorns, B., Goebel, D., and Hofer, R., "Plasma Perturbations in High-Speed Probing of Hall Thruster Discharge Chambers: Quantification and Mitigation," *Presented at the 51st AIAA Joint Propulsion Conference, Orlando, FL, July 27-29, 2015. AIAA-2015-4006.*.

[20]Jorns, B., Hofer, R., and Mikellides, I., "Power Dependence of the Electron Mobility Profile in a Hall Thruster," *Presented at the 50th AIAA Joint Propulsion Conference, Cleveland, OH, July 28-30, 2014. AIAA-2014-3620.*.

[21]Chen, F. F., "Langmuir probe diagnostics," *Mini-Course on Plasma Diagnostics, IEEE-ICOPS Meeting, Jeju, Korea*, 2003.

[22]Fruchtman, A., Zoler, D., and Makrinich, G., "Potential of an emissive cylindrical probe in plasma," *Phys. Rev. E*, Vol. 84, Aug 2011, pp. 025402.

[23]Manzella, D. H., Park, B., and Park, B., "Stationary Plasma Thruster Ion Velocity Distribution," *30th AIAA/ASME/SAE/ASEE Joint Propulsion Conference, Indiana, IN. June 27-29, 1994, AIAA-94-3141*.

[24]Pollard, J. E. and Beiting, E. J., "Measurements of xenon ion velocities of the SPT-140 using laser induced fluorescence," *3rd International Conference on Spacecraft Propulsion. ESA-SP-465, Oct 2000, 789-797.*, 2000.

[25]Hargus, Jr., W. and Cappelli, M., "Laser-induced fluorescence measurements of velocity within a Hall discharge," *Applied Physics B*, Vol. 72, No. 8, 2001, pp. 961–969.

[26]Dorval, N., Bonnet, J., Marque, J. P., Rosencher, E., Chable, S., Rogier, F., and Lasgorceix, P., "Determination of the ionization and acceleration zones in a stationary plasma thruster by optical spectroscopy study: Experiments and model," *Journal of Applied Physics*, Vol. 91, No. 8, 2002.

[27]Gawron, D., Mazouffre, S., Sadeghi, N., and Hron, A., "Influence of magnetic field and discharge voltage on the acceleration layer features in a Hall effect thruster," *Plasma Sources Science and Technology*, Vol. 17, No. 2, 2008, pp. 025001.

[28]Mazouffre, S., Kulaev, V., and Luna, J. P., "Ion diagnostics of a discharge in crossed electric and magnetic fields for electric propulsion," *Plasma Sources Science and Technology*, Vol. 18, No. 3, 2009, pp. 034022.

[29]Spektor, R., Diamant, K. D., Beiting, E. J., Raitses, Y., and Fisch, N. J., "Laser induced fluorescence measurements of the cylindrical Hall thruster plume," *Physics of Plasmas*, Vol. 17, No. 9, 2010.

[30]MacDonald, N. A., Cappelli, M. A., Gildea, S. R., Martnez-Snchez, M., and Jr, W. A. H., "Laser-induced fluorescence velocity measurements of a diverging cusped-field thruster," *Journal of Physics D: Applied Physics*, Vol. 44, No. 29, 2011, pp. 295203.

[31]Huang, W., Gallimore, A. D., and Smith, T. B., "Interior and Near-Wall Ion Velocity Distribution Functions in the H6 Hall Thruster," *Journal of Propulsion and Power*, Vol. 29, No. 5, July 2013, pp. 1146–1154.

[32]Durot, C. J., Gallimore, A. D., and Smith, T. B., "Validation and evaluation of a novel time-resolved laser-induced fluorescence technique," *Review of Scientific Instruments*, Vol. 85, No. 1, 2014.

[33]MacDonald, N. A., Cappelli, M. A., and Jr, W. A. H., "Time-synchronized continuous wave laser-induced fluorescence axial velocity measurements in a diverging cusped field thruster," *Journal of Physics D: Applied Physics*, Vol. 47, No. 11, 2014, pp. 115204.

[34]Huang, W., Smith, T. B., and Gallimore, A. D., "Obtaining Velocity Distribution using a Xenon Ion Line with," *40th AIAA Plasmadynamics and Laser Conference San Antonio, Texas, 22-25 Jun, 2009. AIAA 2009-4226*.

[35]Pawelec, E., Mazouffre, S., and Sadeghi, N., "Hyperfine structure of some near-infrared Xe i and Xe II lines," *Spectrochimica Acta - Part B Atomic Spectroscopy*, Vol. 66, No. 6, 2011, pp. 470–475.

[36]Jorns, B. A. and Hofer, R. R., "Plasma oscillations in a 6-kW magnetically shielded Hall thruster," *Physics of Plasmas*, Vol. 21, No. 5, 2014.

[37]Mikellides, I. G. and Katz, I., "Numerical simulations of Hall-effect plasma accelerators on a magnetic-field-aligned mesh," *Physical Review E*, Vol. 86, No. 4, Oct. 2012, pp. 046703.

[38]Lopez Ortega, A. and Mikellides, I. G., "The importance of the cathode plume and its interactions with the ion beam in numerical simulations of Hall thrusters," *Physics of Plasmas*, Vol. 23, No. 4, 2016.

[39]Yamamura, Y. and Shindo, S., "An empirical formula for angular dependence of sputtering yields," *Radiation Effects*, Vol. 80, No. 1-2, 1984, pp. 57–72.